Nanoscale

PAPER

View Article Online
View Journal

Open Access Article. Published on 13 November 2025. Downloaded on 1/20/2026 2:31:24 AM.
This article is licensed under a Creative Commons Attribution 3.0 Unported Licence.

Check for updates

Cite this: DOI: 10.1039/d5nr04200c

Quantum dot or not? The effect of ligands on the nature of excitations in CdS nanoparticles

Eimear Madden and Martijn A. Zwijnenburg *

We investigate using many-body perturbation theory the optical and electronic properties of neutral cadmium sulfide nanoparticles with the zinc blende structure for which the surface is capped with bisulfide or alkylthiolate ligands, alone or in combination with phosphine, phosphine oxide or amine ligands. We study the nature of the optical excitations for these particles and how the optical and electronic properties of these particles change with the size of their inorganic core. We demonstrate that for all families of particle studied, except those where the corners are capped with aromatic ligands, the optical gap, the onset of light absorption, blue shifts with decreasing particle-core size. For the particles where the corners are capped with alkyl phosphines, phosphine oxides or amines the optical gap is predicted to correspond to an excitation where both the hole and excited electron are delocalised over the inorganic core of the particle, a core-to-core bulk-like excitation, and hence resemble the cartoon picture of a quantum dot. In contrast, we predict that for particles exclusively capped with bisulfide or alkylthiolate ligands, the optical gap corresponds to a charge-transfer excitation with the hole localised on a subset of ligands and only the excited-electron delocalised over the inorganic core of the particle. For particles where the corners are capped with aromatic ligands the optical gap is predicted to correspond to a ligand-to-ligand excitation, which because of its localised nature does not significantly shift with particle size. However for these particles with aromatic ligands, core-to-core excitation, lie only slightly higher in energy, and these excited states will shift with particle size and will likely become the optical gap for large(r) particles. Moreover, as core-to-core excitations are predicted to be much more intense than ligand-to-ligand excitations, experimentally one is likely to observe a blue shift with particle size even for particle sizes where the optical gap technically is a ligand-to-ligand excitation.

Received 3rd October 2025,
Accepted 10th November 2025

DOI: 10.1039/d5nr04200c

rsc.li/nanoscale

Introduction

Nanoparticles made from semiconducting materials, for example cadmium sulfide or indium phospide, which crystallise in the wurtzite or zinc blende/sphalerite crystal structures, typically display a characteristic blue shift of the absorption and/or fluorescence spectra with decreasing nanoparticle size.[1] This blue shift of the spectra of such nanoparticles, often referred to as quantum dots, is both of fundamental scientific and practical interest. The ability to tune the absorption and fluorescence spectrum of nanoparticles by changing the particle size is exploited in the application of such nanoparticles in for example medical imaging,[2] as light absorbing material in solar cells,[3,4] as light emitting material in both light emitting diodes (LEDs) and displays,[5,6] and in the gain media of lasers.[7] Moreover, related materials where nanoparticles of semiconducting materials are grown in an insulating glass matrix or a matrix of another semiconductor are also used as gain media in lasers and in LEDs.[8]

In contrast to nanoparticles of materials that crystallise in the rocksalt structure, wurtzite or zinc blende nanoparticles are not simply cuts from the bulk. Stoichiometric wurtzite or zinc blende cuts have large number of ions with very low coordination numbers and hence are not particularly stable. As a matter of fact, global optimisation studies of stoichiometric clusters of materials such as zinc or cadmium sulfide predict bubble-like global minima that do not resemble fragments of the bulk crystal structure.[9–14] Cuts from the bulk crystal structure, from which all low-coordinated ions have been removed, are generally non-stoichiometric and as a result highly charged. For example, a tetrahedral cut from the zinc blende structure would have twice as many sulfur ions than metal ions and a charge of −20 (see Fig. 1A). Such highly charged particles would probably undergo Coulomb explosion when in the gas phase, and even in solution, where the dielectric qualities of the solvent would screen the charge, would unlikely be stable. Nanoparticles of wurtzite or zinc blende materials hence are generally grown experimentally in the

Department of Chemistry, University College London, 20 Gordon Street, London WC1H 0AJ, UK. E-mail: m.zwijnenburg@ucl.ac.uk

Open Access Article. Published on 13 November 2025. Downloaded on 1/20/2026 2:31:24 AM.
This article is licensed under a Creative Commons Attribution 3.0 Unported Licence.

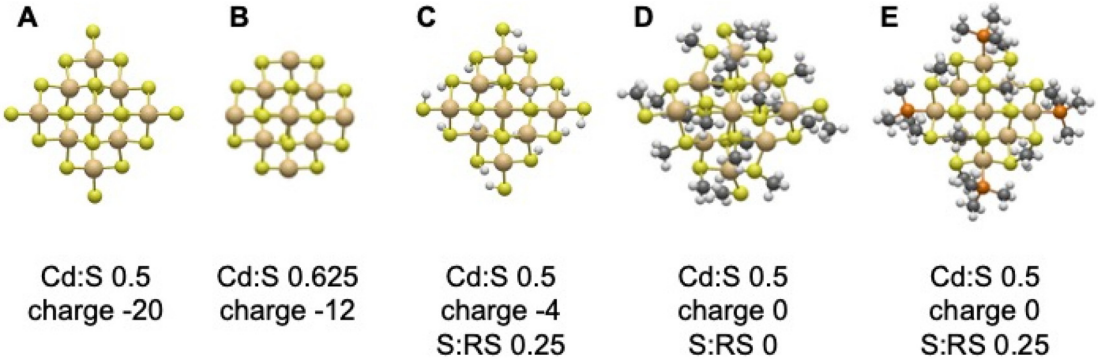

Fig. 1 (A) Tetrahedral cut from the zinc blende structure; (B) tetrahedral cut with the pendant 1-coordinated sulfur anions removed; (C) tetrahedral cut where the 1-coordinated sulfur anions and the 2-coordinated sulfur anions on the edges of the particle have been replaced by X-type bisulfide ligands; (D) tetrahedral cut where all the 1- and 2-coordinated sulfur anions, as well as the 3-coordinated sulfur anions on the face of the particle, have been replaced by methylthiolate X-type ligands; (E) tetrahedral cut where all the 2-coordinated and some 3-coordinated sulfur anions have been replaced by methylthiolate X-type ligands while the 1-coordinated sulfur anions were replaced by neutral trimethylphosphine L-type ligands. Below each particle the cadmium : sulfur ratio, charge and bisulfide/alklylthiolate : sulfur ratio of the structure is shown.

presence of a combination of neutral ligands and charged ligands to increase the coordination of the metal ions on the surface, and in the latter case, reduce the charge on the particle (see Fig. 1C–E), as well as control growth and nucleation rates.[15] Examples of neutral ligands include phosphines and phosphine oxides, while charged ligands are either $XR^{(n-1)-}$ anions, where X^{n-} is the anion of the material in question, for example SR^- thiolates or SH^- bisulfide, or other monoanions such as carboxylates or halides. In the literature, neutral ligands that coordinate through a lone-pair are generally labelled as L-type ligands and anionic ligands as X-type ligands, following the classification scheme of ligands developed by Green[16] and adapted to nanoparticles by Owen.[17]

While generally the structure of large ligand-capped nanoparticles of wurtzite or zinc blende materials is not known with atomic resolution, small atomically precise nanoparticles have been crystallised and X-ray diffraction shows that these particles are indeed generally cuts of the bulk crystal structure, with all metal ions on the corner of the particles coordinated by neutral L-type or $XR^{(n-1)-}$ X-type ligands and all the X^{n-} ions on the edges of particles replaced by $XR^{(n-1)-}$ X-type ligands.[18–24] These small atomically precise nanoparticles are also, as expected generally non-stoichiometric and often negatively charged, crystallising typically as salts with suitable counterions.

When a semiconductor absorbs light excited electron hole pairs, often referred to as excitons, are formed. The excited electrons and holes in these excitons are bound by their mutual coulombic interaction. In bulk semiconductors, the interaction between excited electron and holes is typically small due to the efficient dielectric screening of charges in such materials. Hence, the excitons readily fall apart into free electrons and holes, the free charge carriers. As a result, the room-temperature optical absorption spectra of many bulk semiconductors show no signs of excitons, the signatures of which only show up at low temperature where there is not enough thermal energy to dissociate the excitons. In semiconductor nanostructures, dielectric screening is less efficient and as a result excitons are typically more strongly bound and their optical absorption spectra, even at room temperature, are dominated by excitonic effects. The onset of light absorption, the longest-wavelength lowest-energy light absorbed by a material, is referred to as the optical gap. The minimum energy required to generate a free electron and hole, rather than an exciton, is the fundamental gap (see Fig. S2), often referred to as the band gap in the case of bulk crystalline solids. In the bulk semiconductors mentioned above, the difference between the fundamental/band and optical gap, the exciton binding energy, is small and on the order of K_BT at room temperature (26 meV). In contrast, for nanoparticles the fundamental gap is considerably larger than the optical gap with exciton binding energies values of typically ~10–100 times K_BT.

The blue shift of the optical gap and rest of the optical absorption spectra of semiconductor nanoparticles with decreasing particle size is typically described in terms of the confinement to the particles' volume of both the free charge carriers and the excitons. Analytical models for this have been derived starting from either the effective mass approximation or using particle in a sphere solutions as basis.[25,26] Such analytical models predict that the fundamental gap varies as $1/r^2$ with the particle size r and that the exciton binding energy, or at least its coulombic part, varies as $1/r$. The optical gap, as the fundamental gap minus the exciton binding energy, is predicted by the same models to vary as $1/r^n$, where n varies with particle size, but always has a value between 2 and 1. However, such a description and the derivation of the analytical models based on it assumes uniform and homogeneous particles with a bulk-like electronic structure, which seems a questionable assumption for realistic ligand capped zinc blende and wurtzite particles. Moreover, while in hydrogenated silicon nanoparticles excited-states are indeed deloca-

 This journal is © The Royal Society of Chemistry 2025

Open Access Article. Published on 13 November 2025. Downloaded on 1/20/2026 2:31:24 AM.
This article is licensed under a Creative Commons Attribution 3.0 Unported Licence.

lised over the volume of the particles,[27] work on rocksalt CdO and CdS nanoparticles suggest that even if they display a blue shift of the lowest optically excited state (the optical gap) upon decreasing particle size, the relevant state is only delocalised over the surface rather than the bulk of these otherwise rather uniform and homogeneous particles.[28]

Computational chemistry calculations on realistic models of nanoparticles which include ligands allow us to go beyond the limitation of analytical models and explicitly probe the effect of structural inhomogeneity. Such calculations also provide a way to probe not only the energy of the lowest excited states and how they change with particle size, but also the underlying (de)localisation of the excited states, which is difficult if not impossible to probe by experiment. Calculations also have the advantage that one knows the particles' exact structure by construction and that it is thus possible to compare like with like, untangling effects of particle size from composition, which can be challenging experimentally.

Density functional theory, DFT, and its time-dependent extension, time-dependent DFT, TD-DFT, would be the natural framework to perform calculations on nanoparticles, owing to their favourable scaling with system size. However, with practical exchange–correlation functionals, TD-DFT struggles with the description of so-called charge-transfer states, excited states where the excited electron and hole formed are spatially separated,[29,30] and previous work suggests such states are common for inorganic nanoparticles. TD-DFT calculations can reproduce experimental absorption spectra, for example for magnesium oxide nanoparticles,[31] or the results of high-level quantum chemistry calculations, for example in the case of titanium dioxide clusters,[32,33] however, this requires for each system a careful selection of the exchange–correlation functional in general and tuning the amount of exact exchange in the functional used in particular to minimize issues with charge-transfer states. Moreover, functional tuning often needs to be combined with a rigid red shift of the predicted spectra, as TD-DFT calculations with exchange–correlation functionals that predict the correct energetic ordering of charge-transfer and non-charge-transfer states often spuriously shift the whole spectrum into the blue. In general, such calculations are hence much more empirical than desired. High-level quantum chemistry calculation, such as equation-of-motion coupled cluster calculations, do not suffer from the drawbacks of TD-DFT but do not scale sufficiently favourably with system size to make calculations on real nanosystems computationally tractable. *GW*-BSE many-body perturbation theory calculations based on Green's functions on top of DFT, where *GW*[34–36] is used to calculate the quasiparticle spectra and the Bethe–Salpeter equation[37–39] is solved using the predicted quasiparticle spectra as input to predict the exciton or optical absorption spectra, similarly does not suffer from the drawbacks of TD-DFT. However, in contrast to high-level quantum chemistry methods, *GW*-BSE scales sufficiently favourable with system size, even if still much more computationally expensive than TD-DFT, such that calculations on real nanosystems with *GW*-BSE are computationally tractable. In the literature *GW*-BSE calculations on nanoparticles of one nanometre or larger have been reported for among other materials silicon,[27,40–42] magnesium oxide,[43] cadmium oxide,[28] and cadmium chalcogenides.[28,44–46] *GW*-BSE additionally has as advantage that it treats the quasiparticle and exciton spectra on a similar footing. This allows one to predict internally consistent exciton binding energies and thus the extent by which excitons are stabilised relative to an unbound excited electron and hole, which is difficult for TD-DFT. While there have been limited studies of nanoparticles of CdS and related chalcogenides with the wurtzite or zinc blende structures using *GW*-BSE,[44–46] there has been extensive prior work studying them with (TD-)DFT.[47–57]

In this study we propose structural models for a range of different CdS zinc blende nanoparticles and use *GW*-BSE to study the trend in the predicted optical gap and the (de)localisation of the underlying excited-state with particle size, as well as the same trends for the fundamental gap and the exciton binding energy. After having studied anionic particles where all sulfur ions on the edges and corners of the particles have been replaced by SR^- phenylthiolate ligands in a previous study,[46] we here consider neutral thiolate-terminated zinc blende CdS nanoparticles as models for neutral CdS nanoparticles. These particles are obtained from their anionic counterparts by also replacing a fraction of the otherwise 3-coordinated S^{2-} ions on the faces of the nanoparticles by methyl thiolate/bisulfide X-type ligands. These particles are related to the sodium salts of the anionic nanoparticles previously studied using *GW*-BSE by Zhu *et al.*[45] We also consider neutral particle in which the pendant thiolate or bisulfide X-type ligands on the corners of the particles have been replaced by neutral phosphine, phosphine oxide or pyridine L-type ligands, inspired by the experimental use of such ligands[15,21,58–64] in the synthesis of zinc and cadmium chalcogenide nanostructures. By considering this range of particles and ligands we do not only explore the effect of particle size but also the effect of the exact surface passivation.

Methodology

Starting structures for the neutral thiolate-terminated nanoparticles were obtained from cuts from the experimental bulk CdS structure and/or the experimentally reported X-ray structures of atomically precise nanoparticles. In the case of the bulk cuts all the 2-coordinated S^{2-} ions on the edges of the bulk cuts and a fraction of the 3-coordinated S^{2-} ions on the faces were replaced by SR^- bisulfide or methyl thiolate X-type ligands and the undercoordinated metal ions on the corner of the bulk cuts coordinated by either additional bisulfide or methyl thiolate X-type ligands or trimethylphosphine, triphenyl phosphine, trimethylphosphine oxide, or pyridine L-type ligands. Alternatively, when starting from bulk cuts with 1-coordinated pendant S^{2-} anions, these are replaced with X- or L-type ligands. When starting from the experimentally reported structures of atomically precise nanoparticles the

Open Access Article. Published on 13 November 2025. Downloaded on 1/20/2026 2:31:24 AM.
This article is licensed under a Creative Commons Attribution 3.0 Unported Licence.

X-/L-type ligands of the nanoparticles were replaced by bisulfide, methylthiolate or one of the L-type ligands discussed above if needed, and a fraction of the 3-coordinated S^{2-} ions on the faces replaced by SR^- bisulfide or methyl thiolate X-type ligands in order to obtain neutral particles. The DFT geometry optimisation calculations were performed using the B3LYP[65–67] hybrid exchange–correlation functional in combination with the D4[68] dispersion correction and the def2-SV(P), def2-SVP or def2-TZVPP basis-set.[69] For selected smaller particles frequency calculations were performed to confirm that the respective stationary points found are minima rather than saddle points. All these calculations, as well as the *GW* and BSE calculations discussed below, were performed using Turbomole 7.5.[70]

The quasiparticle spectra of the particles were calculated using *GW* starting from the B3LYP Kohn–Sham orbitals. These calculations were either single shot *GW*, G_0W_0, or eigenvalue self-consistent *GW*, ev*GW*, calculations, where the ev*GW* results are discussed in the main text and the G_0W_0 results are reported in the SI. In these calculations the self-energy is calculated using analytical continuation[71–73] and only the highest occupied and lowest unoccupied quasiparticle states are calculated explicitly using *GW* while the remainder of the quasiparticle states are the Kohn–Sham states (or more correctly the generalised Kohn–Sham states as B3LYP is a hybrid functional) shifted accordingly. In previous work[27,46] we found that this approach yields similar results to when using a spectral representation and explicitly calculating all quasiparticle states with GW but for a fraction of the computational cost. The lowest optical excited states were calculated by solving the Bethe–Salpeter equation on top of the *GW* quasiparticle spectrum.[74]

For G_0W_0 and by extension G_0W_0-BSE the predicted properties will depend on the functional used in the underlying DFT calculation, here B3LYP. The use of ev*GW* instead of G_0W_0 significantly reduces this starting-point dependency by iterating the eigenvalues until self-consistency is achieved. Moreover, in the case of finite-sized systems, such as the CdS particles studied here, the results of ev*GW*-BSE are found to agree well with coupled-cluster benchmarks, as explicitly shown for singlet excitation energies of organic molecules,[71] and yield excitation energies there that are clearly superior to those obtained from G_0W_0-BSE.

The character of the quasiparticle states is analysed in terms of the underlying Kohn–Sham states. The character of the optical excited states, the excitons, is analysed in terms of the corresponding natural transition orbitals (NTOs),[75] as well as a series of descriptors developed by Plasser and co-workers, such as the root mean square electron–hole separation and the CT character.[76–79] The latter analysis is performed using the TheoDORE code.[80]

The qualitative delocalisation of the excitons is analysed in terms of how many atoms in the inorganic core of the particles contribute more than $\sum q_i/N$ to the hole or electron component of the exciton, as well as the maximum value of $q_i/\sum q_i$ for either the hole or electron component. Here, N is the total number of atoms in the core, q_i the contribution of atom i to the electron or hole component of the exciton as calculated by TheoDORE, $\sum q_i$ the contribution of all the atoms in the core summed (equal to one if the exciton is fully located on the core), $\sum q_i/N$ the contribution each atom would have if each atom would contribute equally and $q_i/\sum q_i$ the contribution of atom i as a fraction of the sum. We also calculate the participation ratio (PR) for the hole and excited electron components of the excitons, which we define following Alexander and co-workers[81] and Llusar and co-workers[57] as:

$$\mathrm{PR} = (\sum q_i)^2/(N\sum q_i{}^2) \tag{1}$$

where the PR value, defined as such, varies between $1/N$ for a state fully localised on one atom of the core and 1 for a state fully delocalised over the core. We are aware that in the literature the results of eqn (1) are sometimes referred to as the inverse participation ratio (IPR)[56] but we believe PR to be the more correct terminology as it corresponds to the ratio of the atoms participating in an excited state and the total number of atoms. Other authors[55] discuss instead the true IPR, which obviously equals the inverse of the result of eqn (1), but appear to plot PR. We also calculate the product of PR and N, which is measure of the number of atoms involved with the hole or excited electron component of the exciton. This product of PR and N, finally, also equals the participation ratio as reported by TheoDORE,[82] in which case N is defined more generally as the number of subsystems.

Fourier transforms of the (natural transition) orbitals are obtained to probe the 'reciprocal space' nature of the orbitals using an inhouse python code[83] built around the NumPy library and with a cube file of the (natural transition) orbitals as input. The Fourier transforms are plotted as a function of k_x and k_y defined as:

$$K_i = 2\pi/l_i \tag{2}$$

and plotted in terms of:

$$G = 2\pi/a_0 \tag{3}$$

where a_0 is the bulk lattice parameter of the primitive unit-cell of zinc blende CdS. With the information along the z-direction projected on the xy plane by summing up the contributions along the z-axis for each k_xk_y value.

The properties of the particles are all plotted relative to the radius R of the inorganic core of the particles. R is calculated from the average edge length of the inorganic cores L assuming the particles are ideal tetrahedra as the distance between the centroid of the particle and the vertices:

$$R = (3/8)^{0.5} \times L \tag{4}$$

Results

Properties of the $[Cd_{10}S_{20}]^{20-}$ cut derived particles

Having checked the basis-set convergence (see section I of the supplementary discussion in the SI), we start our discussion here by considering the optical and electronic properties of

 This journal is © The Royal Society of Chemistry 2025

Open Access Article. Published on 13 November 2025. Downloaded on 1/20/2026 2:31:24 AM.
This article is licensed under a Creative Commons Attribution 3.0 Unported Licence.

the CdS nanoparticles. We initially focus our discussion on the different particles that can be derived from a $[Cd_{10}S_{20}]^{20-}$ cut from the CdS zinc blende structure, as these particles are both relatively small and have relatively high symmetry (see Fig. 2 and Fig. S3 in the SI). These nanoparticles include the neutral $[Cd_{10}(SR)_{20}]$ particle in which all the twenty 1-, 2- and 3-coordinated sulfur ions have been replaced by thiolate or bisulfide X-type ligands and the neutral $[Cd_{10}S_4(SR)_{12}L_4]$ particle in which the four pendant 1-coordinated sulfur ions have been replaced by neutral L-type ligands and the sixteen 2-coordinated sulfur ions by thiolate or bisulfide X-type ligands. There is also the anionic $[Cd_{10}S_4(SR)_{16}]^{4-}$ particle in which all the sixteen 1- and 2-coordinated sulfur ions have been replaced by thiolate or bisulfide X-type ligands, which we have already studied in previous work, mentioned above.[46] This anionic $[Cd_{10}S_4(SR)_{16}]^{4-}$ nanoparticle has been prepared experimentally as an atomically precise nanoparticles in the case of phenylthiolate and crystallised as a salt with alkylammonium counterions.[18,19] Similarly, the zinc analogue of the neutral $[Cd_{10}S_4(SR)_{12}L_4]$ particle has been experimentally prepared[21] as an atomically precise nanoparticles using ethylthiolate and 3,5-lutidine or pyridine as the neutral L-type ligand.

Table 1 gives the predicted fundamental and optical gap values for the different neutral Cd_{10} particles. From the data it is clear that the $[Cd_{10}(SR)_{20}]$ particle with either bisulfide or methylthiolate X-type ligands consistently has smaller fundamental and optical gaps than the neutral $[Cd_{10}S_4(SR)_{12}L_4]$ particle, independent of the exact nature of the L-type ligand. The anionic phenylthiolate $[Cd_{10}S_4(SPh)_{16}]^{4-}$ particle, the only anionic Cd_{10} particle for which basis-set convergence is likely not an issue (see our previous work[46] and the SI), has a fundamental gap that is similar to the $[Cd_{10}S_4(SR)_{12}L_4]$ particles but an optical gap that is smaller than all the neutral particles. The exciton binding energy for all neutral Cd_{10} particles are similar but the excited-state for the anionic phenylthiolate $[Cd_{10}S_4(SPh)_{16}]^{4-}$ particle is considerably stronger bound. Calculations with the larger def2-TZVPP basis-set, where tractable, finally, give very similar results to those using the smaller def2-SVP basis-set.

Table 1 evGW-BSE predicted properties of the different neutral $[Cd_{10}S_{20}]^{20-}$ cut derived particles. All values in eV and obtained with the def2-SVP basis-set except the values in parentheses that were obtained with the larger def2-TZVPP basis-set. Data for $[Cd_{10}S_4(SPh)_{16}]^{4-}$ taken from our previous work.[46] The equivalent G_0W_0 data can be found in Table S9 in the SI

	Δ_F	Δ_O	EBE
$[Cd_{10}(SMe)_{20}]$	6.61	3.94	2.67
$[Cd_{10}(SH)_{20}]$	6.88 (6.80)	4.01 (4.01)	2.87 (2.79)
$[Cd_{10}S_4(SMe)_{12}(TMP)_4]$	7.35	4.56	2.78
$[Cd_{10}S_4(SH)_{12}(TMP)_4]$	7.26 (7.15)	4.45 (4.41)	2.81 (2.73)
$[Cd_{10}S_4(SMe)_{12}(TMPO)_4]$	7.36	4.58	2.79
$[Cd_{10}S_4(SMe)_{12}(TPP)_4]$	7.30	4.50	2.80
$[Cd_{10}S_4(SMe)_{12}(Py)_4]$	7.22	4.69	2.54
$[Cd_{10}S_4(SPh)_{16}]^{4-}$	6.61	3.12	3.49

Character of the lowest excited states for $[Cd_{10}S_{20}]^{20-}$ cut derived particles

The character of the lowest excited states in different Cd_{10} particles was examined by analysing the (de)localisation of the

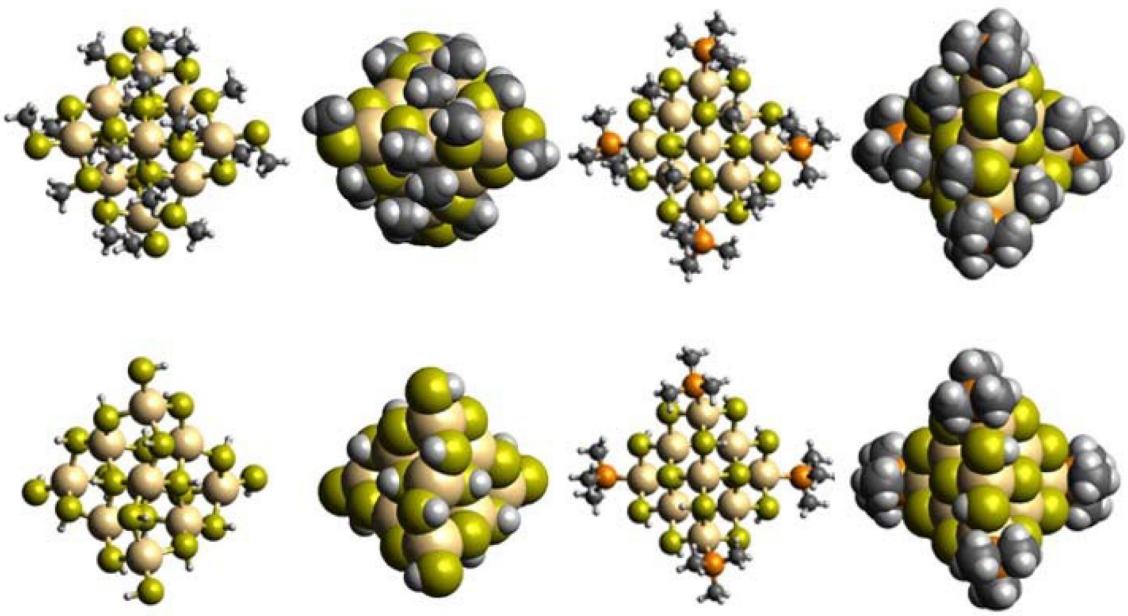

Fig. 2 DFT optimised structure of the $[Cd_{10}(SMe)_{20}]$ particle (top left), $[Cd_{10}(SH)_{20}]$ particle (bottom left), $[Cd_{10}S_4(SMe)_{12}(TMP)_4]$ particle (top right) and $[Cd_{10}S_4(SH)_{12}(TMP)_4]$ particle (bottom right), where for each particle the structure is shown in a ball-and-stick representation and with the atoms rendered as van der Waals spheres. Fig. S3 in the SI additionally shows the DFT optimised structure of $[Cd_{10}S_4(SMe)_{12}(TPP)_4]$.

Open Access Article. Published on 13 November 2025. Downloaded on 1/20/2026 2:31:24 AM.
This article is licensed under a Creative Commons Attribution 3.0 Unported Licence.

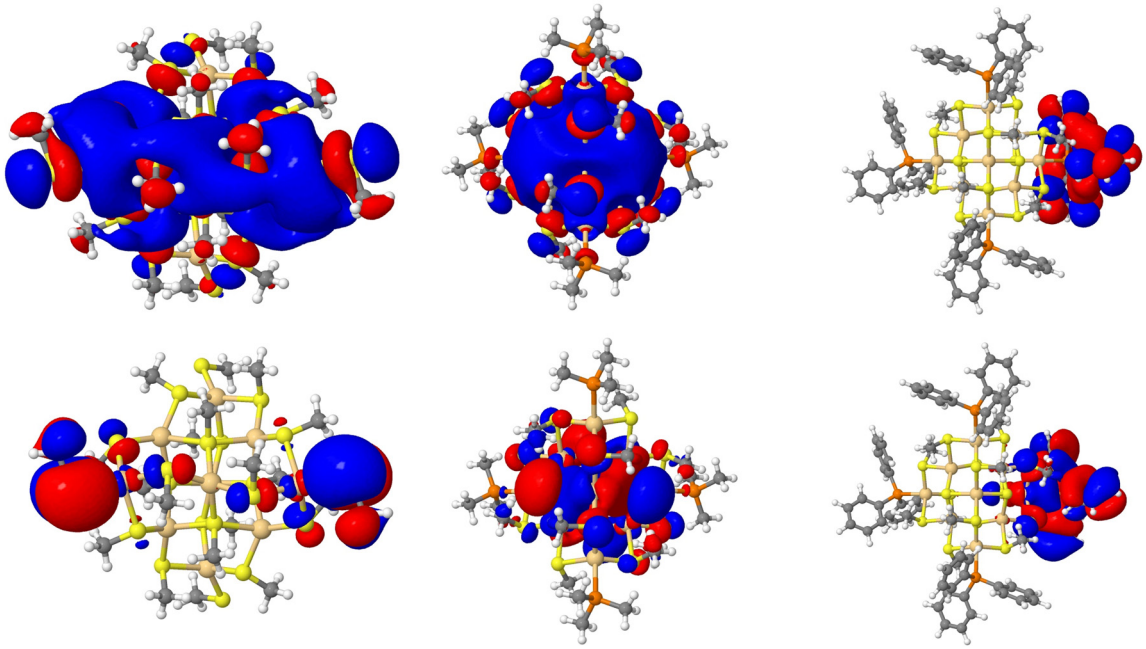

Fig. 3 Pictures of the occupied (bottom row) and virtual (top row) component of the leading natural transition orbital for the lowest excitation corresponding to the optical gap of the $[Cd_{10}(SMe)_{20}]$ (left), $[Cd_{10}S_4(SMe)_{12}(TMP)_4]$ (middle) and $[Cd_{10}S_4(SMe)_{12}(TPP)_4]$ (right).

electron and hole components across various regions of the nanoparticles. This was assessed using the TheoDORE code[80] and inferred from the (de)localisation patterns of the dominant natural transition orbitals (see Fig. 3). Based on this analysis, the lowest excited state of neutral $[Cd_{10}(SR)_{20}]$ nanoparticles (capped exclusively with methylthiolate or bisulfide ligands) exhibits partial charge-transfer character, with the hole localised on the corner-capping X-type ligands and the excited electron delocalised primarily over the inorganic core, with some extension to the corner ligands. This localisation is similar to what we observed in our previous work on the phenylthiolate capped anionic particles.[46] In contrast, for the neutral trimethylphosphine, trimethylphosphine oxide or trimethylamine corner capped $[Cd_{10}S_4(SR)_{12}L_4]$ nanoparticles the lowest excited state is located on the inorganic core of the nanoparticles with minimal contribution of the corner-capping L-type ligands, *i.e.* a true core-to-core excitation. The hole is mostly delocalised over the sulfur ions of the cores and the excited electron is roughly equally shared between the cadmium and sulfur ions in the core. This aligns with the bulk, where the valence band maximum is predominantly sulfur-derived, while the conduction band minimum has contributions from both sulfur and cadmium. Finally, the excited state corresponding to the optical gap of the neutral $[Cd_{10}S_4(SR)_{12}L_4]$ nanoparticles where the corner-capping L-type ligand is an aromatic ligand (triphenylphosphine, pyridine) is nearly exclusively localised on the corner-capping L-type ligand in the case of triphenylphosphine ($[Cd_{10}S_4(SMe)_{12}TPP_4]$) and predominantly on the corner-capping L-type ligand with minor contributions of the cadmium ion that the pyridine is coordinated to and the adjacent sulfur ions in the case of pyridine ($[Cd_{10}S_4(SMe)_{12}Py_4]$). For these particles the optical gap can best be described as primarily a π to π^* ligand-to-ligand excitation even if the fundamental and optical gap values of these particles are very similar to those with alkylphosphine (oxide) L-type ligands. Hence only in the case of the neutral $[Cd_{10}S_4(SR)_{12}L_4]$ nanoparticles with alkyl corner-capping L-type ligands does the optical gap corresponds to a bulk-like excitation purely localised on the inorganic core. This is also the only case where the optical gap is predicted to correspond to an excitation with significant oscillator strength.

Character of higher excited states for $[Cd_{10}S_{20}]^{20-}$ cut derived particles

For the neutral $[Cd_{10}S_4(SR)_{12}L_4]$ particles with aromatic corner-capping L-type ligands, core-to-core excitations lie higher in energy, approximately 0.5 eV higher than the optical gap in the case of triphenylphosphine. For their alkyl counterparts, the higher energy excitations in the same energy window, in contrast, do not drastically change in character. However, the hole component of the exciton does become increasingly more delocalised over the inorganic core (see Fig. S4 and section II of the supplementary discussion in the SI). Similarly, for $[Cd_{10}(SR)_{20}]$ the electron component of the higher energy excitons are more delocalised over the core of the particle but the hole localisation on the corner capping X-type ligands remains the same. At even higher energies, the excitations for $[Cd_{10}(SR)_{20}]$ finally start to have partial core-to-core character but there always remains a significant localisation of the hole on the pendant corner-capping X-type ligands (see Fig. S4 and section II of the supplementary discussion in the SI).

 This journal is © The Royal Society of Chemistry 2025

Open Access Article. Published on 13 November 2025. Downloaded on 1/20/2026 2:31:24 AM.
This article is licensed under a Creative Commons Attribution 3.0 Unported Licence.

TD-DFT *vs.* ev*GW*-BSE

As TD-DFT has, as discussed in the introduction, been previously used to study the optical properties of CdS particles, it is interesting to see how the predictions of TD-DFT compares to those by ev*GW*-BSE. For $[Cd_{10}S_4(SR)_{12}(TMP)_4]$ TD-DFT calculations with a range of different exchange–correlation functionals agree with ev*GW*-BSE in terms of the predicted character of its lowest excited state, see section III of the supplementary discussion in the SI. However, none of the functionals tested in the TD-DFT calculations reproduce the ev*GW*-BSE predicted character of the lowest excited state for both $[Cd_{10}(SMe)_{20}]$ and $[Cd_{10}S_4(SR)_{12}(TPP)_4]$. Moreover, where TD-DFT predicts a different character of the lowest excited-state than ev*GW*-BSE, this is typically not a case of the energetic ordering of lowest excited states being inverted, but TD-DFT instead predicting excited-states with a character not observed among any of the lowest energy ev*GW*-BSE predicted excited states.

Change with particle size

Having discussed the properties of the Cd_{10} particles we will now explore the effect of changing particle size on the fundamental gap, optical gap and exciton binding energy values for the different classes of particles. We will do so by discussing the results of calculations on the neutral $[Cd_{10}(SR)_{20}]$, $[Cd_{20}S_5(SR)_{30}]$ and $[Cd_{35}S_{14}(SR)_{42}]$, and $[Cd_{10}S_4(SR)_{12}L_4]$, $[Cd_{20}S_9(SR)_{22}L_4]$ and $[Cd_{35}S_{18}(SR)_{34}L_4]$ particles. Just as for Cd_{10} the other larger particles can be derived from the corresponding bulk cuts by replacing the four 1-coordinated pendant sulfur ions by thiolate or bisulfide X-type or neutral L-type ligands, all the 2-coordinated sulfur ions by thiolate or bisulfide X-type ligands, and a fraction of the 3-coordinated sulfur ions by thiolate or bisulfide X-type ligands (see Fig. 4). In these larger neutral particles only a fraction of the 3-coordinated sulfur ions are replaced by thiolate or bisulfide X-type ligands. This in contrast to $[Cd_{10}(SR)_{20}]$, where all 3-coordinated sulfur ions have been replaced by a thiolate or bisulfide X-type ligand, and $[Cd_{10}S_4(SR)_{12}L_4]$, where none of the 3-coordinated sulfur ions are replaced. As a result, there will be many isomers for the larger particles differing in which exact subset of 3-coordinated sulfur ions are replaced. The number of these isomers increases dramatically with particle size, which means we can focus on only a small number of more ordered isomers below.

Fig. 5 shows the variation of the fundamental and optical gap with the size of the inorganic core for the different classes of particles studied. Fig. 6 also shows for each of the classes of particles a fit of the predicted fundamental and optical gap values to

$$\Delta_{F/O} = a + b/r^n \tag{5}$$

where a, b and n are constants and where we fix a to be the experimental band gap of bulk zinc blende CdS, 2.5 eV.[84] Eqn (5) has been previously successfully used by us[27] and others[85–87] to describe the variation of the fundamental and optical gap values of semiconductor nanoparticles such as silicon with particle size. As can be seen from Fig. 5 for each set of particles studied here the fundamental and optical gap are predicted to increase with decreasing size of the inorganic core of the particles, *i.e.* to blue shift, irrespective of the char-

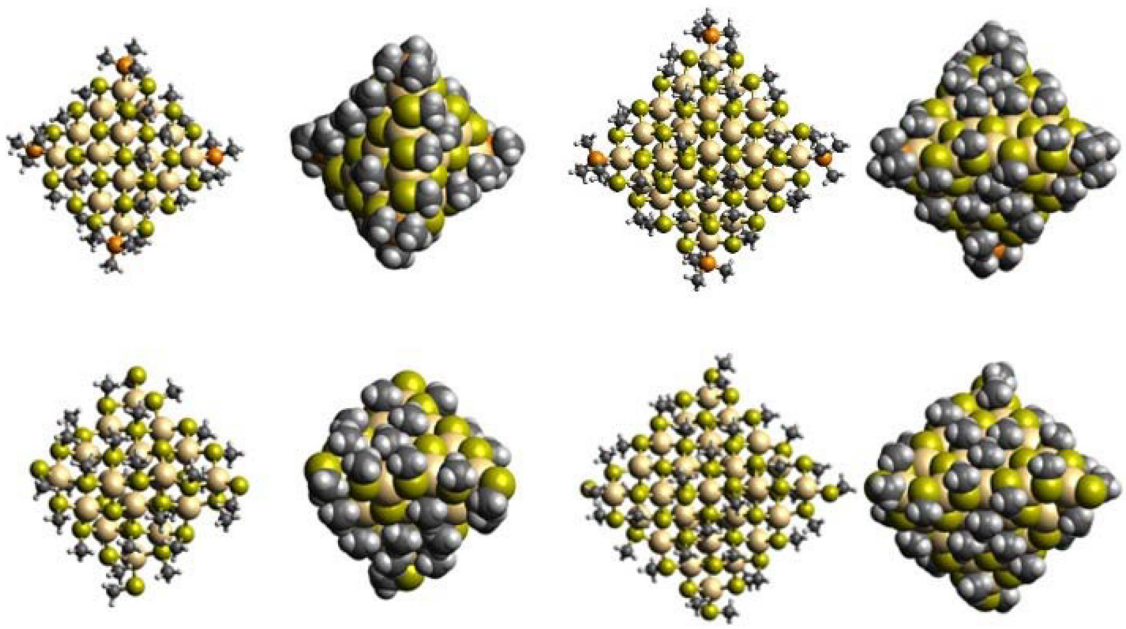

Fig. 4 DFT optimised structure of the $[Cd_{20}S_9(SMe)_{22}(TMP)_4]$ particle (top left), $[Cd_{35}S_{18}(SMe)_{34}(TMP)_4]$ particle (top tight), $[Cd_{20}S_5(SMe)_{30}]$ particle (bottom left) and $[Cd_{35}S_{14}(SMe)_{42}]$ particle (bottom right), where for each particle the structure is shown in a ball-and-stick representation and with the atoms rendered as van der Waals spheres.

Open Access Article. Published on 13 November 2025. Downloaded on 1/20/2026 2:31:24 AM.
This article is licensed under a Creative Commons Attribution 3.0 Unported Licence.

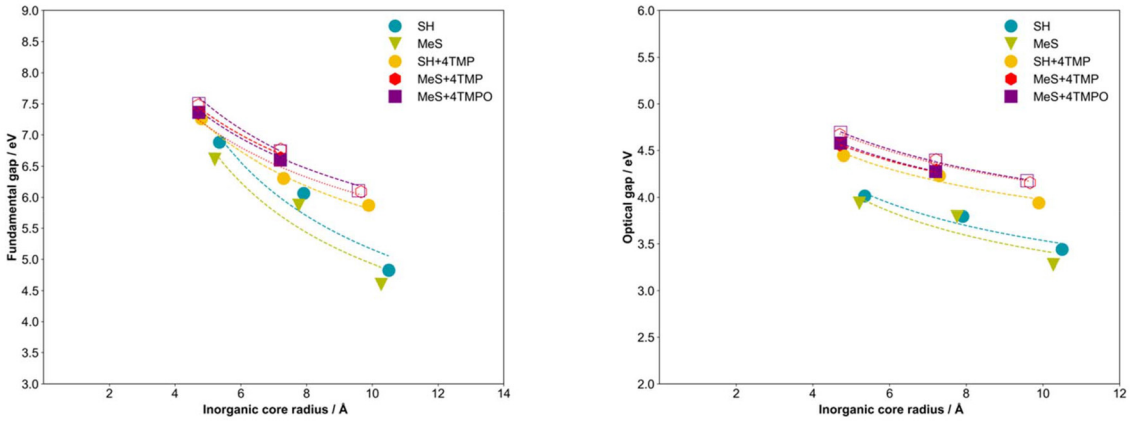

Fig. 5 Plot of the predicted fundamental gap (left) and optical gap (right) for the different particles *versus* the radius of the inorganic cores of the particles. The dashed lines correspond fits of the data to eqn (5). Closed symbols calculated with the def2-SVP basis-set and open symbols using the def2-SV(P) basis-set. The underlying data can be found in Tables S10–S15 in the SI.

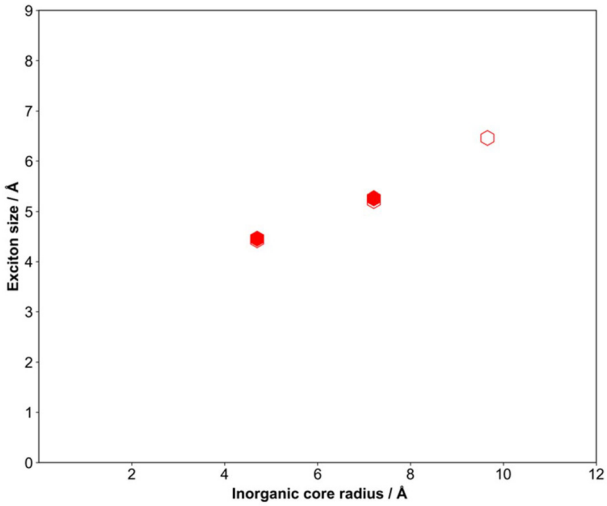

Fig. 6 Plot of the exciton radius of trimethylphoshpine corner capped particles *versus* the radius of the inorganic core. Closed symbols calculated with the def2-SVP basis-set and open symbols using the def2-SV(P) basis-set. For the two smaller particles the def2-SVP and def2-SV(P) data points overlap.

acter of the underlying excitation in the case of the optical gap. Also, for most classes of particles, except perhaps the methylthiolate terminated neutral particles, the predicted fundamental and optical gap values fit well to eqn (5). The fit parameters for each class of particles can be found in Tables S16–S19 in the SI. Just as for the hydrogenated silicon nanoparticles[27] the fitted n values are both in the case of the fundamental and optical gap values for the different families of particles smaller than the values expected from simple analytical models. Ranging from 0.4 to 0.8 instead of 2 in the case of the fundamental gap and ranging between 0.3 and 0.8 instead of between 1 and 2 for the optical gap.

Similarly to the fundamental and optical gap values, the predicted exciton binding energy values increase with decreasing size of the particle's inorganic core, see Fig. S5, demonstrating that as expected excitons are more strongly bound in the particles than for the bulk. These values can also be fitted to an equation similar to eqn (5), with a fixed to 0 in the case of the exciton binding energy, assuming for simplicity that the excitons in bulk CdS have negligible binding energy (see Tables S20 and S21 in the SI). We are not aware of measurements or predictions of the exciton binding energy in bulk zinc blende CdS, but the experimentally reported bulk exciton binding energy for the wurtzite polymorph of CdS is 29 meV (0.029 eV),[88] which indeed is negligible compared to the values predicted for the particles.

Particles with aromatic corner-capping ligands

As discussed above, for $[Cd_{10}S_4(SR)_{12}L_4]$ with aromatic L-type ligands the lowest excited state corresponding to the optical gap is a ligand-to-ligand excitation with excitations predominantly involving the inorganic core lying higher in energy. The size of the aromatic ligands and the scaling of the ev*GW*/BSE calculations with system size means we cannot explore the same size range as for the smaller alkyl ligands. However, we were able to run evGW/BSE calculations for $[Cd_{20}S_9(SMe)_{22}TPP_4]$. Comparing the results of the calculation with those for $[Cd_{10}S_4(SMe)_{12}TPP_4]$ shows that the optical gap barely shifts when going from $[Cd_{10}S_4(SMe)_{12}TPP_4]$ to $[Cd_{20}S_9(SMe)_{22}TPP_4]$ but that the lowest core-to-core excitation, *i.e.* the lowest excitation that is predominantly localised on the core, shifts down by more than 0.2 eV (see Table S22 in the SI). These results suggest that the character of the lowest excited state of neutral particles with aromatic corner-capping L-type ligands will eventually change with increasing particle size, and that for larger particles it will end up being predominantly located on the inorganic core. Moreover, as the predicted oscillator strength of core-to-core excitations is at least one order of magnitude larger than for the ligand-to-ligand transition, it is likely that also in advance of the transition, the most intense,

 This journal is © The Royal Society of Chemistry 2025

Open Access Article. Published on 13 November 2025. Downloaded on 1/20/2026 2:31:24 AM.
This article is licensed under a Creative Commons Attribution 3.0 Unported Licence.

red-shifted experimental absorption feature of these particles will correspond to a core-to-core excitation.

Particles without corner-capping ligands

As the corner-capping L-type ligands are relatively weakly bound, one can imagine particles without them. Indeed, Houtepen and co-workers[55,57] have previously studied the (de) localisation of the DFT orbitals of CdSe particles with 3-co-ordinated cadmium ions as proxy for their quasiparticle states. We calculated the optical and electronic properties of $[Cd_{10}S_4(SR)_{12}]$, $[Cd_{20}S_9(SR)_{22}]$ and $[Cd_{35}S_{18}(SR)_{34}]$ particles starting from the geometries of their lowest energy $[Cd_{10}S_4(SR)_{12}L_4]$, $[Cd_{20}S_9(SR)_{22}L_4]$ and $[Cd_{35}S_{18}(SR)_{34}L_4]$ counterparts and found that their predicted properties were very similar (see Table S23), including the delocalisation of the hole and excited electron components of the excitons over the core of the particles.

Delocalisation in real space and exciton size

Focussing in on the particles with trimethylphosphine L-type ligands coordinated to the corner cadmium ions as examples of neutral particles with non-aromatic L-type ligands, Fig. 6 plots the exciton size, defined as the root mean square separation between the electron and hole component of the exciton as calculated in the TheoDORE code,[79,80] *versus* the radius of the inorganic core of the particles. Fig. 6 shows that the exciton size increases approximately linearly with the particle size, in line with what would be expected from an exciton delocalised over the volume of the inorganic core. However, it is also apparent that the predicted exciton size for the $[Cd_{20}S_9(SMe)_{22}(TMP)_4]$ and $[Cd_{35}S_{18}(SMe)_{34}(TMP)_4]$ particles are clearly smaller than the corresponding core radii, and that the difference between the core radius and exciton size appears to increase with increasing core radius. We observe the same for hydrogen-terminated silicon nanoparticles.[27] However, the slope of the correlation between exciton size and particle size/core radius is approximately 25% smaller for the CdS particles compared to that for the silicon particles. For the same particle/core radius, the excitons in the CdS particles are thus predicted to be smaller than those in the silicon particles. This all is in line with the (de)localisation of the leading natural transition orbital for the lowest excitations of the $[Cd_{20}S_9(SMe)_{22}(TMP)_4]$ and $[Cd_{35}S_{18}(SMe)_{34}(TMP)_4]$ particles, as shown in Fig. S6 and S7, which are delocalised over the volume of the inorganic core, just not the whole volume of the core. In contrast, for the hydrogen terminated silicon nanoparticles the relevant natural transition orbitals appear delocalised over the whole particle volume.[27]

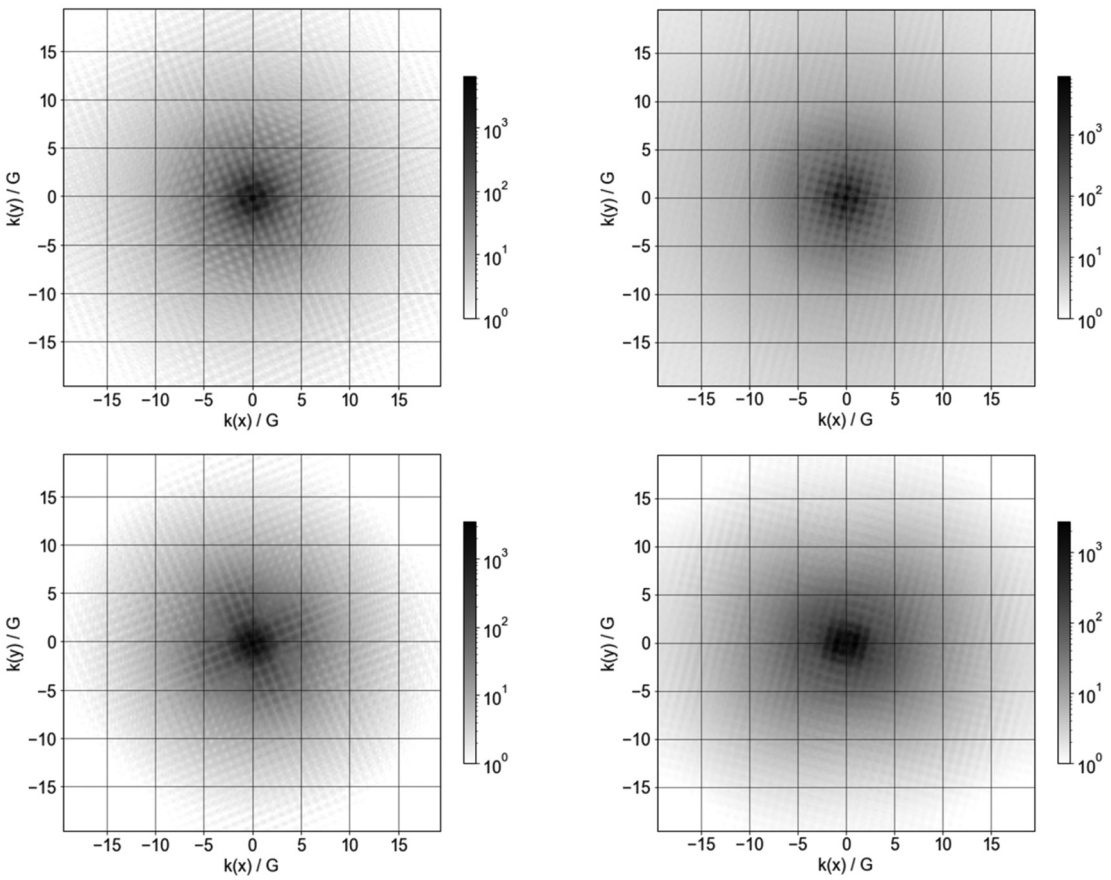

Fig. 7 Fourier transforms of the orbitals corresponding to the highest occupied (bottom) and lowest unoccupied quasiparticle (top) states of $[Cd_{10}S_4(SME)_{12}(TMP)_4]$ (left) and $[Cd_{35}S_{18}(SMe)_{34}(TMP)_4]$ (right).

Open Access Article. Published on 13 November 2025. Downloaded on 1/20/2026 2:31:24 AM.
This article is licensed under a Creative Commons Attribution 3.0 Unported Licence.

We can also analyse the (de)localisation of the (lowest energy) exciton for the different particles in terms of how many atoms in the inorganic core of the particles contribute more than $\sum q_i/N$ to the hole or electron component of the exciton, the maximum contribution $q_i/\sum q_i$ of an atom to either and the PR (participation ratio) value, similar as is done for the Cd_{10} particles in section II of the supplementary discussion in the SI. Table S24 shows that when going from $[Cd_{10}S_4(SMe)_{12}(TMP)_4]$ to $[Cd_{35}S_{18}(SMe)_{34}(TMP)_4]$ the number of atoms in the core with a contribution of more than $\sum q_i/N$ to the hole or electron component of the lowest energy exciton for these particles increases approximately linearly with core radius but that the hole is delocalised over only ~20% of the atoms the core and the electron over ~30–40% of the atoms. All in line with the plots of the relevant natural transition orbitals discussed above. The product of PR and N (see Table S25) for the same particles also increases approximately linearly for the excited electron component but for the hole component displays a less clear trend. Slightly higher energy excitons can be more delocalised, involving for example 25–40% of the atoms in the core for the hole component and ~40% of the atoms in case of the excited electron component and with lower $\max(q_i/\sum q_i)$ values and higher PR × N product values (see Tables S26, S27 and Fig. S8). Finally, all low energy excitations for the alkyl phosphine capped particles are fundamentally similar in character, *i.e.* core-to-core excitations. There is no evidence of other types of excitations coming down in energy with changing particle size. This in contrast to the case of the aromatic L-type ligands discussed above.

Taking particles capped only with methylthiolate as an example of particles exclusively capped with X-type ligands then we observe something similar though slightly more complicated. As can be seen from Table S28 a similar number of atoms in the cores of $[Cd_{10}(SMe)_{20}]$ and $[Cd_{20}S_5(SMe)_{30}]$ make a significant contribution to the excited electron component of the lowest energy exciton and the maximum $q_i/\sum q_i$ contribution of the latter is nearly double the former. While the doubling of the maximum $q_i/\sum q_i$ contribution is an artefact of the symmetry of $[Cd_{10}(SR)_{20}]$, and the fact that the contribution of symmetry equivalent atoms is the same, it is clear that the size of the lowest energy exciton does not significantly change when going from $[Cd_{10}(SMe)_{20}]$ to $[Cd_{20}S_5(SMe)_{30}]$. However, the excited electron component of the lowest energy exciton for $[Cd_{35}S_{14}(SMe)_{42}]$ is significantly more delocalised, involving 3–4 times more atoms than for $[Cd_{10}(SMe)_{20}]$ and $[Cd_{20}S_5(SMe)_{30}]$ and a maximum $q_i/\sum q_i$ value that is 3.5 to 7.5 times smaller. This (increased) delocalisation is also apparent from the natural transition orbitals for the lowest energy excited state of $[Cd_{35}S_{14}(SMe)_{42}]$, which are shown in Fig. S8 in the SI. The PR × N values paint a similar picture (see Table S29). There is some evidence that excitations with partial core-to-core character are coming down in energy with increasing particle size, but these excitations remain blue-shifted with respect to the optical gap by more than 0.5 eV in the size range studied.

Delocalisation in reciprocal space

We also performed a Fourier transform of the Kohn–Sham orbitals corresponding the highest occupied and lowest unoccupied quasiparticle states of the $[Cd_{10}S_4(SR)_{12}L_4]$ and $[Cd_{35}S_{18}(SR)_{34}L_4]$ particles, as well as for the hole and electron component of the leading natural transition orbitals (see Fig. 7 and Fig. S9), to probe the 'reciprocal space' nature of the (natural transition) orbitals. We use quotation marks around reciprocal space here because the wavevector k is not a proper quantum number for nanoparticles due to their finite size.

In contrast to silicon nanoparticles, the pattern of spots in the Fourier transforms is similar for the occupied and unoccupied quasiparticle state, in line with the fact that bulk CdS is a direct gap semiconductor and not an indirect semiconductor like silicon. However, similar to the silicon nanoparticles, we see the same pattern of spots for the Kohn–Sham orbitals corresponding to the highest occupied and lowest unoccupied quasiparticle states and the natural transition orbitals. The natural transition orbitals, and thus the corresponding lowest energy excitons, appear to have inherited the periodicity of the frontier orbitals, and thus the periodicity of the underlying atomic structure of the particles. Finally, considering Fig. 7 and Fig. S9, it is apparent that in contrast to for silicon nanoparticles the pattern of spots does not become more focussed with increasing particle size, but instead becomes more diffuse. This is possibly due to the methyl bisulfide or methylthiolate ligands replacing only a part of the surface sulfur ions for the larger particles and as a result perturbing the symmetry of the core.

Discussion

Effect of ligands on the character of the excitons

The nature of the corner-capping ligands is clearly critical in deciding the character of the (lowest energy) exciton(s) in the neutral CdS nanoparticles. As described above, in the case that the corner-capping ligand is an alkylthiolate or bisulfide X-type ligand, the lowest energy exciton is consistently predicted to be a charge-transfer state with the hole localised on the corner-capping ligand and the electron delocalised over the inorganic core of the particle. When alkylphosphine, phosphine oxide, or amine L-type ligands cap the corner of the particles, we predict that the lowest-energy exciton is delocalised over the inorganic core. Similarly, in the absence of a ligand coordinated to the corner cadmium atoms, now 3- instead of 4-coordinated, the lowest-energy exciton is delocalised over the inorganic core. Finally, for the particle size-range studied, the lowest energy exciton is localised on the aromatic ligand when the corner-capping ligand is an aromatic phosphine, phosphine oxide or amine L-type ligand. However, core-to-core excitation, similar as for with particles with alkyl L-type corner-capping ligands, lie for these particles with aromatic ligands only slightly higher in energy and with increasing particle size these delocalised states shift down in energy and may eventually end up becoming the lowest energy excited states. For

 This journal is © The Royal Society of Chemistry 2025

Open Access Article. Published on 13 November 2025. Downloaded on 1/20/2026 2:31:24 AM.
This article is licensed under a Creative Commons Attribution 3.0 Unported Licence.

CdS nanoparticles the ligands are thus typically not electronically innocent, and the choice of ligands experimentally is important beyond their role in synthesis and providing stability against aggregation. Similarly, when modelling such CdS nanoparticles it is clear one needs to be careful with simplifying ligands to accelerate calculations.

Surface or bulk states

In the literature the excitations of nanoparticles of cadmium chalcogenide and related materials and the underlying quasiparticle states are often described as either surface or bulk excitons/states depending on their degree of delocalisation and the atoms involved.[48,54–57,81] Another criterium used to distinguish surface and bulk states in the case of quasiparticle states is if they are midgap states or not, which we discuss in supplementary discussion IV in the SI. The lowest excited state for the particles with aromatic L-type corner-capping ligands where both the hole and excited electron component of the exciton are localised on the corner ligand clearly can be described as a surface state, as this excited state wouldn't exist in the absence of the surface. Similarly, following the same logic, the lowest excited state for the particles exclusively capped with alkylthiolate or bisulfide X-type ligands should be described as a surface state, as again the hole is localised on one or more of the corner-capping ligands, even if the excited electron component is to a greater or lesser degree delocalised over the inorganic core.

Goldzak and coworkers[56] find that the hole component of the lowest energy excitons for the wurtzite CdSe particles they study using TD-DFT strongly localise on 2-coordinated selenium ions on the surface of the particles and thus can be classified as surface states. While the cores of the zinc blende particles we study here lack these 2-coordinated chalcogen ions, having been replaced by bisulfide/thiolate ions, they are in effect reintroduced when capping the corners with alkylthiolate or bisulfide X-type ligands. As such, even if the origin and nature of the 2-coordinated chalcogens is different, we agree that 2-coordinated chalcogen ions give rise to surface states.

The lowest excited states for the particles with non-aromatic L-type corner-capping ligands, in contrast, do not, as discussed above, significantly involve the ligands and more importantly the hole and especially the excited electron component are delocalised over a significant number of atoms making these arguably bulk rather than surface states. This is clearest for the higher energy excitons as for those the hole is delocalised over (even) more atoms. The lowest excited state for the particles with 'naked' corners, *i.e.* where the L-type corner-capping ligands have been removed, finally, behave like their counterparts with L-type corner-capping ligands, and also can be classified as bulk rather than surface states.

Evidence for quantum confinement

For all the classes of CdS nanoparticles studied here, other than those with aromatic corner-capping L-type ligands, the optical gap clearly increases with decreasing particle size and the optical gap values of the particles are clearly larger than for the bulk. Naively, this could be seen as evidence for quantum confinement. However, the (de)localisation of the lowest energy exciton in the different classes of particles, discussed above, is rather different than the textbook cartoon picture of quantum confinement, other for than the particles with L-type corner-capping ligands, and even in that case delocalisation is not over the whole core. For example, in the neutral particles with bisulfide and methylthiolate corner-capping X-type ligands, only the excited electron is delocalised over the inorganic core and not both the hole and excited electron. Most of the hole is not even located on the inorganic core but the on the ligand instead. That said, it stands to reason that the confinement of the delocalised excited electron component of the exciton to the volume of the inorganic core probably is responsible for the predicted downward shift of the optical gap with increasing particle size in these particles. The case of nanoparticles with triphenylphosphine as corner-capping L-type ligands, where the lowest energy exciton in the size range studied is predicted to be purely localised on the ligand and where the optical gap remains nearly constant, provides a clear example of how fully localised excitons do not exhibit size-dependent shifts.

Absorption and fluorescence intensity

The core-to-core excitations in which both the hole and excited electron component of the exciton are delocalised over the inorganic core are predicted to have oscillator strengths that are at least one order of magnitude larger than those corresponding to charge-transfer or ligand-to-ligand excitations. As discussed above, this is the reason that even if the lowest energy exciton for small nanoparticles with aromatic corner-capping ligands is ligand-based, and hence the lowest excitation energy does not significantly shift with particle size, one could still experimentally observe a shift in the spectrum. That shift is then due to higher energy core-to-core states, which are more intense and do shift with particle size. The relative darkness of the excited states corresponding to the lowest energy excitons for the particles exclusively capped with alkyl thiolate or bisulfide X-type ligands also means that such particles should have relatively long fluorescence lifetimes, provided there is no efficient non-radiative de-excitation mechanism, which might be of practical interest, or alternatively a low fluorescence intensity when non-radiative decay is efficient. Indeed, for CdSe particles it was previously observed[89] through post-synthesis ligand exchange that particles with X-type ligands capping the surface have lower fluorescence intensities than those with L-type ligands. Phenylthiolate terminated CdS nanoparticles, or particles with aromatic phosphines, phosphine oxides or amines as corner-capping ligands in the size-range where the lowest excited state is ligand based, are also predicted to have long fluorescence lifetimes or low fluorescence intensities. However, for such the particles the localisation of the exciton on the ligands means that long fluorescence lifetimes/low fluorescence intensities in those cases would be more a property of those ligands than a property of

Open Access Article. Published on 13 November 2025. Downloaded on 1/20/2026 2:31:24 AM. This article is licensed under a Creative Commons Attribution 3.0 Unported Licence.

the inorganic core or an emergent property of the combination of inorganic core and ligands.

'Reciprocal space' character

The periodicity in 'reciprocal space' for both the Kohn–Sham orbitals corresponding to the highest occupied and lowest unoccupied quasiparticle state and the electron and hole component of the natural transition orbitals for the neutral particles with trimethylphosphine or trimethylphosphine oxide ligands, suggest that such particles do not only inherit the atomic structure but also the electronic structure of the bulk CdS. The reciprocal space periodicity combined with the delocalisation of exciton in real space suggests that, just as for hydrogenated silicon nanoparticles, the excitons in these particles are just like in the bulk CdS large radius Wannier-Mott excitons and not small radius Frenkel excitons, as suggested by the large exciton binding energy. Similar as for hydrogenated silicon nanoparticles,[27] the large exciton binding energy is likely a consequence of reduced dielectric screening in nanoparticles compared to the bulk.

Comparison with experiment

The optical gap values predicted here, and their trends, can be compared to measurements for experimentally synthesized nanoparticles. Probably, the best comparison for the neutral methylthiolate terminated particles is the data by Vossmeyer and co-workers[90] who prepared CdS particles with a radius of 6–50 Å in the presence of 1-thioglycerol and report their absorption spectra and optical gap values. Their data and the trend they observe with particle size agrees well with our predicted values. This becomes especially clear when plotting our optical gap data *versus* a measure of the radius of the particles that includes the sulfur atoms of the corner-capping ligands, and the experimental optical gap data in the same plot (see Fig. S10 in the SI). Above we define the size of the particles in Fig. 5 and 6 in terms of just the core of the particle and specifically the distance between the terminal cadmium atoms (see eqn (4)), as that allows one to plot data for particles with different corner capping ligands along the same *x*-axis. However, the experimental radii reported by Vossmeyer and co-workers are obtained from small-angle X-ray scattering and hence contain at least some contribution of the ligands to the extracted radii, if not only from the ligand's sulfur atoms, and for like-to-like comparison require a measure of the radius of the particles that includes the sulfur atoms of the corner-capping ligands.

For the phosphine/phosphine oxide corner capped particles the best comparison perhaps is the experimental data of Bansal and co-workers[62] who synthesize CdS nanoparticles with the zinc blende structure in the presence of both a deprotonated alkyl thiol (octanethiol) X-type ligand and a range of L-type ligands (trioctylphosphine oxide, trioctylphosphine, diphenylphosphine). The experimental data of Bansal and co-workers not only shows a blue shift of the onset of light absorption with decreasing particle size, in line with that predicted here for alkyl phosphine (oxide) corner capped particles, but the optical gap values of the smallest particles are also similar to those predicted here for approximately similar sized particles. Specifically, the $[Cd_{35}S_{18}(SR)_{34}L_4]$ particles have a core radius of 9.6 Å and a evGW-BSE/def2-SV(P) predicted optical gap of 4.16–4.18 eV, depending on the exact L-type ligand, while the smallest CdS nanoparticles of Bansal and co-workers have an estimated ~9 Å radius and an optical gap of ~3.55 eV (350 nm).

Comparison to previous computational studies

Finally, it's worth comparing the predictions here to those in previous computational studies where not already explicitly discussed above. Using G_0W_0-BSE, Zhu and co-workers[45] previously studied neutral bisulfide capped CdS nanoparticles with additional sodium cations adsorbed on some of the sulfur ions on the faces of the particles to charge compensate the net negative charge of the core. These particles are analogues of the neutral bisulfide capped particles studied here other than that they have a mixed wurtzite-zinc blende core instead of pure zinc blende cuts. The optical gaps predicted by Zhu and co-workers are similar to those in Fig. 7 and again show a similar trend with particle size. However, the fundamental gap values and exciton binding energies predicted by Zhu and co-workers are considerably smaller. The latter is most likely the result of their use of G_0W_0 starting from PBE eigenvalues, which preserves the underestimation of the fundamental gap inherent to generalised gradient approximation functionals such as PBE. One can also compare the predictions for tetrahedral CdS nanoparticles here to those for octahedral rocksalt CdS nanoparticles studied in our previous work.[28] In rocksalt CdS nanoparticles the lowest energy exciton is predicted to be delocalised, but only over the surface of the particle and not its volume. The addition of amine ligands coordinating to cadmium ions on the surface of the particles was not found to change that prediction. It is tempting to attribute this difference in exciton localisation to the likely more ionic bonding in the rocksalt polymorph, which would suggest a lower electronic-only static dielectric constant and reduced dielectric screening. However, if anything, calculations for the bulk predict the opposite,[91] with zinc blende CdS predicted to have a lower electronic-only static dielectric constant than the rocksalt polymorph.

Conclusions

The optical properties of ligand terminated zinc blende cadmium sulfide nanoparticles are found to strongly depend on the exact nature of the ligand. The ligands are found to often not be innocent spectators but actively involved in low-energy excitations including the optical gap. Only for nanoparticles with alkyl phosphines, phosphine oxides or amines as corner-capping L-type ligands is the optical gap predicted to correspond to an excitation that is primarily delocalised over the inorganic core with minimal contribution of the ligands, a core-to-core bulk-like excitation. For particles with aromatic

 This journal is © The Royal Society of Chemistry 2025

Open Access Article. Published on 13 November 2025. Downloaded on 1/20/2026 2:31:24 AM.
This article is licensed under a Creative Commons Attribution 3.0 Unported Licence.

corner-capping L-type ligands, the optical gap is predicted to correspond to a ligand-to-ligand excitation even if excited states delocalised over the inorganic core lie only slightly higher in energy. Finally, for particles with bisulfide or alkylthiolates as corner-capping X-type ligands, the optical gap and all low energy excitations correspond to a charge-transfer excitation between the ligands and the inorganic core.

For all studied nanoparticles, the optical gap is predicted to increase with deceasing particle size, except for those particles with aromatic corner-capping ligands, where the optical gap does not significantly change with particle size, in line with the fact that for such ligands the optical gap corresponds to a ligand based excitation. Hence, while a blue shift in the absorption spectra of particles with decreasing particle size, and thus a red shift with increasing particle size, is a clear sign of a delocalised excited state restricted in size by the volume of the particles, it is not a sign that this state necessarily only involves the inorganic core of the particles and is bulk-like. Moreover, while for the particles with aromatic phosphines, phosphine oxides or amines as corner-capping L-type ligands, the optical gap does not shift with particle size, higher energy states delocalised over the inorganic core are predicted to move down in energy with increasing particle size and might become the state corresponding to the optical gap for larger particle sizes. These delocalised states are also predicted to be much brighter than their ligand localised counterparts and hence might result in an observable shift of the absorption spectra for such particles, even when smaller than the size where the optical gap becomes inorganic core based.

The optical gaps for all particles are predicted to correspond to clear excitons with significant exciton binding energies. The large exciton binding energies likely are the result of the reduced dielectric screening for nanoparticles compared to the bulk and not a sign of a small exciton. Indeed, for nanoparticles with alkyl phosphines or phosphine oxides as corner-capping ligands, the excitons are not only delocalised over the inorganic core in real space but also in 'reciprocal space'. The excitons in these nanoparticles, and by extension, the higher-energy delocalised excitons in particles with aromatic phosphines or phosphine oxides, are predicted to be large Wannier-Mott excitons, similar to those in bulk cadmium sulfide.

Conflicts of interest

There are no conflicts to declare.

Data availability

The data supporting this article have been included as part of the supplementary information (SI). Supplementary information: basis-set convergence information, G_0W_0(-BSE) results, TD-DFT results, fitting constants and DFT optimised structures of all relevant particles. See DOI: https://doi.org/10.1039/d5nr04200c.

Acknowledgements

Prof. Brandi Cossairt, Prof. Ivan Infante, Prof. Jan-Ole Joswig, Dr Felix Plasser, Prof. Troy van Voorhis, as well as the attendees of the 2022 Gordon Research Conference on Atomically Precise Nanochemistry are kindly acknowledged for useful discussion. EM acknowledges the UK Engineering and Physical Sciences Research Council (EPSRC) for a DTP studentship (EP/T517793/1).

References

1 A. L. Efros and L. E. Brus, Nanocrystal Quantum Dots: From Discovery to Modern Development, *ACS Nano*, 2021, **15**, 6192–6210.
2 S. Kargozar, S. J. Hoseini, P. B. Milan, S. Hooshmand, H.-W. Kim and M. Mozafari, Quantum Dots: A Review from Concept to Clinic, *Biotechnol. J.*, 2020, **15**, 2000117.
3 G.-H. Kim, F. P. García de Arquer, Y. J. Yoon, X. Lan, M. Liu, O. Voznyy, Z. Yang, F. Fan, A. H. Ip, P. Kanjanaboos, *et al.*, High-Efficiency Colloidal Quantum Dot Photovoltaics Via Robust Self-Assembled Monolayers, *Nano Lett.*, 2015, **15**, 7691–7696.
4 V. T. Chebrolu and H.-J. Kim, Recent Progress in Quantum Dot Sensitized Solar Cells: An Inclusive Review of Photoanode, Sensitizer, Electrolyte, and the Counter Electrode, *J. Mater. Chem. C*, 2019, **7**, 4911–4933.
5 E. Jang and H. Jang, Review: Quantum Dot Light-Emitting Diodes, *Chem. Rev.*, 2023, **126**, 4663–4692.
6 D. Tian, H. Ma, G. Huang, M. Gao, F. Cai, Y. Fang, C. Li, X. Jiang, A. Wang, S. Wang, *et al.*, A Review on Quantum Dot Light-Emitting Diodes: From Materials to Applications, *Adv. Opt. Mater.*, 2023, **11**, 2201965.
7 Y.-S. Park, J. Roh, B. T. Diroll, R. D. Schaller and V. I. Klimov, Colloidal Quantum Dot Lasers, *Nat. Rev. Mater.*, 2021, **6**, 382–401.
8 M. Xia, J. Luo, C. Chen, H. Liu and J. Tang, Semiconductor Quantum Dots-Embedded Inorganic Glasses: Fabrication, Luminescent Properties, and Potential Applications, *Adv. Opt. Mater.*, 2019, **7**, 1900851.
9 E. Spanó, S. Hamad and C. R. A. Catlow, Computational Evidence of Bubble ZnS Clusters, *J. Phys. Chem. B*, 2003, **107**, 10337–10340.
10 E. Spanó, S. Hamad and C. R. A. Catlow, ZnS Bubble Clusters with Onion-Like Structures, *Chem. Commun.*, 2004, 864–865.
11 S. Hamad, C. R. A. Catlow, E. Spanó, J. M. Matxain and J. M. Ugalde, Structure and Properties of ZnS Nanoclusters, *J. Phys. Chem. B*, 2005, **109**, 2703–2709.
12 A. Burnin, E. Sanville and J. J. BelBruno, Experimental and Computational Study of the Z_nnS_n and $Zn_nS_n^+$ Clusters, *J. Phys. Chem. A*, 2005, **109**, 5026–5034.
13 E. Sanville, A. Burnin and J. J. BelBruno, Experimental and Computational Study of Small (N = 1–16) Stoichiometric Zinc and Cadmium Chalcogenide Clusters, *J. Phys. Chem. A*, 2006, **110**, 2378–2386.

Open Access Article. Published on 13 November 2025. Downloaded on 1/20/2026 2:31:24 AM.
This article is licensed under a Creative Commons Attribution 3.0 Unported Licence.

14 M. A. Zwijnenburg, Optical Excitations in Stoichiometric Uncapped ZnS Nanostructures, *Nanoscale*, 2011, **3**, 3780–3787.
15 M. A. Boles, D. Ling, T. Hyeon and D. V. Talapin, The Surface Science of Nanocrystals, *Nat. Mater.*, 2016, **15**, 141–153.
16 M. L. H. Green, A New Approach to the Formal Classification of Covalent Compounds of the Elements, *J. Organomet. Chem.*, 1995, **500**, 127–148.
17 J. Owen, The Coordination Chemistry of Nanocrystal Surfaces, *Science*, 2015, **347**, 615–616.
18 I. G. Dance, A. Choy and M. L. Scudder, Syntheses, Properties, and Molecular and Crystal Structures of $(Me_4N)4[E_4M_{10}(Sph)_{16}]$ (E = Sulfur or Selenium; M = Zinc or Cadmium): Molecular Supertetrahedral Fragments of the Cubic Metal Chalcogenide Lattice, *J. Am. Chem. Soc.*, 1984, **106**, 6285–6295.
19 K. S. Hagen and R. H. Holm, The Stereochemistry of Decakis(Benzenethiolato)Tetracadmate(2-) Ion, a Cage Complex Related to the Cadmium-Cysteinate Aggregates in Metallothioneins, *Inorg. Chem.*, 1983, **22**, 3171–3174.
20 W. E. Farneth, N. Herron and Y. Wang, *Bulk Semiconductors from Molecular Solids: A Mechanistic Investigation*, *Chemistry of Materials*, 1992, vol. 4, pp. 916–922.
21 M. D. Nyman, M. J. Hampden-Smith and E. N. Duesler, Synthesis and Characterization of the First Neutral Zinc–Sulfur Cluster: $Zn_{10}S_4(SEt)_{12}L_4$, *Inorg. Chem.*, 1996, **35**, 802–803.
22 N. Herron, J. C. Calabrese, W. E. Farneth and Y. Wang, Crystal Structure and Optical Properties of $Cd_{32}S_{14}(SC_6H_5)_{36}.Dmf_4$, a Cluster with a 15 Angstrom CdS Core, *Science*, 1993, **259**, 1426–1428.
23 S. Behrens, M. Bettenhausen, A. Eichhöfer and D. Fenske, Synthesis and Crystal Structure of $[Cd_{10}Se_4(SePh)_{12}(PPh_3)_4]$ and $[Cd_{16}(SePh)_{32}(PPh_3)_2]$, *Angew. Chem., Int. Ed. Engl.*, 1997, **36**, 2797–2799.
24 M. W. DeGroot, N. J. Taylor and J. F. Corrigan, Controlled Synthesis of Ternary II–II'–VI Nanoclusters and the Effects of Metal Ion Distribution on Their Spectral Properties, *Inorg. Chem.*, 2005, **44**, 5447–5458.
25 L. E. Brus, Electron–Electron and Electron–Hole Interactions in Small Semiconductor Crystallites: The Size Dependence of the Lowest Excited Electronic State, *J. Chem. Phys.*, 1984, **80**, 4403–4409.
26 L. Brus, Electronic Wave Functions in Semiconductor Clusters: Experiment and Theory, *J. Phys. Chem.*, 1986, **90**, 2555–2560.
27 E. Madden and M. A. Zwijnenburg, The Effect of Particle Size on the Optical and Electronic Properties of Hydrogenated Silicon Nanoparticles, *Phys. Chem. Chem. Phys.*, 2024, **26**, 11695–11707.
28 M. A. Zwijnenburg, The Effect of Particle Size and Composition on the Optical and Electronic Properties of CdO and CdS Rocksalt Nanoparticles, *Phys. Chem. Chem. Phys.*, 2022, **24**, 21954–21965.
29 D. J. Tozer, R. D. Amos, N. C. Handy, B. O. Roos and L. Serrano-Andres, Does Density Functional Theory Contribute to the Understanding of Excited States of Unsaturated Organic Compounds?, *Mol. Phys.*, 1999, **97**, 859–868.
30 M. J. G. Peach, P. Benfield, T. Helgaker and D. J. Tozer, Excitation Energies in Density Functional Theory: An Evaluation and a Diagnostic Test, *J. Chem. Phys.*, 2008, **128**, 044118.
31 M. C. C. Wobbe, A. Kerridge and M. A. Zwijnenburg, Optical Excitation of MgO Nanoparticles; a Computational Perspective, *Phys. Chem. Chem. Phys.*, 2014, **16**, 22052–22061.
32 E. Berardo, H.-S. Hu, S. A. Shevlin, S. M. Woodley, K. Kowalski and M. A. Zwijnenburg, Modeling Excited States in TiO_2 Nanoparticles: On the Accuracy of a TD-DFT Based Description, *J. Chem. Theory Comput.*, 2014, **10**, 1189–1199.
33 E. Berardo, H.-S. Hu, H. J. J. van Dam, S. A. Shevlin, S. M. Woodley, K. Kowalski and M. A. Zwijnenburg, Describing Excited State Relaxation and Localization in TiO_2 Nanoparticles Using TD-DFT, *J. Chem. Theory Comput.*, 2014, **10**, 5538–5548.
34 L. Hedin, New Method for Calculating the One-Particle Green's Function with Application to the Electron-Gas Problem, *Phys. Rev.*, 1965, **139**, A796–A823.
35 F. Aryasetiawan and O. Gunnarsson, The GW Method, *Rep. Prog. Phys.*, 1998, **61**, 237–312.
36 D. Golze, M. Dvorak and P. Rinke, The GW Compendium: A Practical Guide to Theoretical Photoemission Spectroscopy, *Front. Chem.*, 2019, **7**, 377.
37 E. E. Salpeter and H. A. Bethe, A Relativistic Equation for Bound-State Problems, *Phys. Rev.*, 1951, **84**, 1232–1242.
38 G. Strinati, Application of the Green's Functions Method to the Study of the Optical Properties of Semiconductors, *Riv. Nuovo Cimento*, 1988, **11**, 1–86.
39 X. Blase, I. Duchemin, D. Jacquemin and P.-F. Loos, The Bethe–Salpeter Equation Formalism: From Physics to Chemistry, *J. Phys. Chem. Lett.*, 2020, **11**, 7371–7382.
40 C. Delerue, M. Lannoo and G. Allan, Excitonic and Quasiparticle Gaps in Si Nanocrystals, *Phys. Rev. Lett.*, 2000, **84**, 2457–2460.
41 M. L. Tiago and J. R. Chelikowsky, Confinement Effects in the Optical Properties of Semiconductor Nanocrystals, *Phys. Status Solidi B*, 2006, **243**, 2151–2158.
42 D. Rocca, M. Vörös, A. Gali and G. Galli, Ab Initio Optoelectronic Properties of Silicon Nanoparticles: Excitation Energies, Sum Rules, and Tamm–Dancoff Approximation, *J. Chem. Theory Comput.*, 2014, **10**, 3290–3298.
43 M. A. Zwijnenburg, The Effect of Particle Size on the Optical and Electronic Properties of Magnesium Oxide Nanoparticles, *Phys. Chem. Chem. Phys.*, 2021, **23**, 21579–21590.
44 M. Lopez del Puerto, M. L. Tiago and J. R. Chelikowsky, Ab Initio Methods for the Optical Properties of CdSe Clusters, *Phys. Rev. B:Condens. Matter Mater. Phys.*, 2008, **77**, 045404.

 This journal is © The Royal Society of Chemistry 2025

Open Access Article. Published on 13 November 2025. Downloaded on 1/20/2026 2:31:24 AM.
This article is licensed under a Creative Commons Attribution 3.0 Unported Licence.

45 X. Zhu, G. A. Chass, L.-C. Kwek, A. L. Rogach and H. Su, Excitonic Character in Optical Properties of Tetrahedral CdX (X = S, Se, Te) Clusters, *J. Phys. Chem. C*, 2015, **119**, 29171–29177.
46 E. Madden and M. A. Zwijnenburg, Optical Properties of Phenylthiolate-Capped CdS Nanoparticles, *J. Phys. Chem. C*, 2025, **129**, 1797–1805.
47 J. Frenzel, J.-O. Joswig and G. Seifert, Optical Excitations in Cadmium Sulfide Nanoparticles, *J. Phys. Chem. C*, 2007, **111**, 10761–10770.
48 S. Kilina, S. Ivanov and S. Tretiak, Effect of Surface Ligands on Optical and Electronic Spectra of Semiconductor Nanoclusters, *J. Am. Chem. Soc.*, 2009, **131**, 7717–7726.
49 S. V. Kilina, D. S. Kilin and O. V. Prezhdo, Breaking the Phonon Bottleneck in PbSe and CdSe Quantum Dots: Time-Domain Density Functional Theory of Charge Carrier Relaxation, *ACS Nano*, 2009, **3**, 93–99.
50 M. Del Ben, R. W. A. Havenith, R. Broer and M. Stener, Density Functional Study on the Morphology and Photoabsorption of CdSe Nanoclusters, *J. Phys. Chem. C*, 2011, **115**, 16782–16796.
51 O. Voznyy, D. Zhitomirsky, P. Stadler, Z. Ning, S. Hoogland and E. H. Sargent, A Charge-Orbital Balance Picture of Doping in Colloidal Quantum Dot Solids, *ACS Nano*, 2012, **6**, 8448–8455.
52 J. M. Azpiroz and F. De Angelis, Ligand Induced Spectral Changes in CdSe Quantum Dots, *ACS Appl. Mater. Interfaces*, 2015, **7**, 19736–19745.
53 S. V. Kilina, P. K. Tamukong and D. S. Kilin, Surface Chemistry of Semiconducting Quantum Dots: Theoretical Perspectives, *Acc. Chem. Res.*, 2016, **49**, 2127–2135.
54 C. Giansante and I. Infante, Surface Traps in Colloidal Quantum Dots: A Combined Experimental and Theoretical Perspective, *J. Phys. Chem. Lett.*, 2017, **8**, 5209–5215.
55 A. J. Houtepen, Z. Hens, J. S. Owen and I. Infante, On the Origin of Surface Traps in Colloidal II–VI Semiconductor Nanocrystals, *Chem. Mater.*, 2017, **29**, 752–761.
56 T. Goldzak, A. R. McIsaac and T. Van Voorhis, Colloidal CdSe Nanocrystals Are Inherently Defective, *Nat. Commun.*, 2021, **12**, 890.
57 J. Llusar, I. du Fossé, Z. Hens, A. Houtepen and I. Infante, Surface Reconstructions in II–VI Quantum Dots, *ACS Nano*, 2024, **18**, 1563–1572.
58 J. E. B. Katari, V. L. Colvin and A. P. Alivisatos, X-Ray, Photoelectron Spectroscopy of CdSe Nanocrystals with Applications to Studies of the Nanocrystal Surface, *J. Phys. Chem.*, 1994, **98**, 4109–4117.
59 C. B. Murray, D. J. Norris and M. G. Bawendi, Synthesis and Characterization of Nearly Monodisperse CdE (E = Sulfur, Selenium, Tellurium) Semiconductor Nanocrystallites, *J. Am. Chem. Soc.*, 1993, **115**, 8706–8715.
60 M. Lazell and P. O'Brien, Synthesis of CdS Nanocrystals Using Cadmium Dichloride and Trioctylphosphine Sulfide, *J. Mater. Chem.*, 1999, **9**, 1381–1382.
61 N. C. Anderson and J. S. Owen, Soluble, Chloride-Terminated CdSe Nanocrystals: Ligand Exchange Monitored by ^{1}H and ^{31}P NMR Spectroscopy, *Chem. Mater.*, 2013, **25**, 69–76.
62 A. K. Bansal, F. Antolini, S. Zhang, L. Stroea, L. Ortolani, M. Lanzi, E. Serra, S. Allard, U. Scherf and I. D. W. Samuel, Highly Luminescent Colloidal CdS Quantum Dots with Efficient near-Infrared Electroluminescence in Light-Emitting Diodes, *J. Phys. Chem. C*, 2016, **120**, 1871–1880.
63 N. C. Anderson, P. E. Chen, A. K. Buckley, J. De Roo and J. S. Owen, Stereoelectronic Effects on the Binding of Neutral Lewis Bases to CdSe Nanocrystals, *J. Am. Chem. Soc.*, 2018, **140**, 7199–7205.
64 H. H. Ripberger, K. J. Schnitzenbaumer, L. K. Nguyen, D. M. Ladd, K. R. Levine, D. G. Dayton, M. F. Toney and B. M. Cossairt, Navigating the Potential Energy Surface of Cdse Magic-Sized Clusters: Synthesis and Interconversion of Atomically Precise Nanocrystal Polymorphs, *J. Am. Chem. Soc.*, 2023, **145**, 27480–27492.
65 C. Lee, W. Yang and R. G. Parr, Development of the Colle-Salvetti Correlation-Energy Formula into a Functional of the Electron Density, *Phys. Rev. B:Condens. Matter Mater. Phys.*, 1988, **37**, 785–789.
66 A. D. Becke, Density–Functional Thermochemistry. III. The Role of Exact Exchange, *J. Chem. Phys.*, 1993, **98**, 5648–5652.
67 P. J. Stephens, F. J. Devlin, C. F. Chabalowski and M. J. Frisch, Ab Initio Calculation of Vibrational Absorption and Circular Dichroism Spectra Using Density Functional Force Fields, *J. Phys. Chem.*, 1994, **98**, 11623–11627.
68 E. Caldeweyher, S. Ehlert, A. Hansen, H. Neugebauer, S. Spicher, C. Bannwarth and S. Grimme, A Generally Applicable Atomic-Charge Dependent London Dispersion Correction, *J. Chem. Phys.*, 2019, **150**, 154122.
69 F. Weigend and R. Ahlrichs, Balanced Basis Sets of Split Valence, Triple Zeta Valence and Quadruple Zeta Valence Quality for H to Rn: Design and Assessment of Accuracy, *Phys. Chem. Chem. Phys.*, 2005, **7**, 3297–3305.
70 S. G. Balasubramani, G. P. Chen, S. Coriani, M. Diedenhofen, M. S. Frank, Y. J. Franzke, F. Furche, R. Grotjahn, M. E. Harding, C. Hättig, *et al.*, Turbomole: Modular Program Suite for Ab Initio Quantum-Chemical and Condensed-Matter Simulations, *J. Chem. Phys.*, 2020, **152**, 184107.
71 X. Gui, C. Holzer and W. Klopper, Accuracy Assessment of GW Starting Points for Calculating Molecular Excitation Energies Using the Bethe–Salpeter Formalism, *J. Chem. Theory Comput.*, 2018, **14**, 2127–2136.
72 M. J. van Setten, F. Weigend and F. Evers, The GW-Method for Quantum Chemistry Applications: Theory and Implementation, *J. Chem. Theory Comput.*, 2013, **9**, 232–246.
73 C. Holzer and W. Klopper, Ionized, Electron-Attached, and Excited States of Molecular Systems with Spin–Orbit Coupling: Two-Component GW and Bethe–Salpeter Implementations, *J. Chem. Phys.*, 2019, **150**, 204116.

Open Access Article. Published on 13 November 2025. Downloaded on 1/20/2026 2:31:24 AM.
This article is licensed under a Creative Commons Attribution 3.0 Unported Licence.

74 K. Krause and W. Klopper, Implementation of the Bethe–Salpeter Equation in the Turbomole Program, *J. Comput. Chem.*, 2017, **38**, 383–388.
75 R. L. Martin, Natural Transition Orbitals, *J. Chem. Phys.*, 2003, **118**, 4775–4777.
76 S. A. Mewes, J.-M. Mewes, A. Dreuw and F. Plasser, Excitons in Poly(Para Phenylene Vinylene): A Quantum-Chemical Perspective Based on High-Level Ab Initio Calculations, *Phys. Chem. Chem. Phys.*, 2016, **18**, 2548–2563.
77 F. Plasser, M. Wormit and A. Dreuw, New Tools for the Systematic Analysis and Visualization of Electronic Excitations. I. Formalism, *J. Chem. Phys.*, 2014, **141**, 024106.
78 F. Plasser, S. A. Bäppler, M. Wormit and A. Dreuw, New Tools for the Systematic Analysis and Visualization of Electronic Excitations. II. Applications, *J. Chem. Phys.*, 2014, **141**, 024107.
79 S. A. Bäppler, F. Plasser, M. Wormit and A. Dreuw, Exciton Analysis of Many-Body Wave Functions: Bridging the Gap between the Quasiparticle and Molecular Orbital Pictures, *Phys. Rev. A*, 2014, **90**, 052521.
80 F. Plasser, Theodore: A Toolbox for a Detailed and Automated Analysis of Electronic Excited State Computations, *J. Chem. Phys.*, 2020, **152**, 084108.
81 E. Alexander, M. Kick, A. R. McIsaac and T. Van Voorhis, Understanding Trap States in InP and GaP Quantum Dots through Density Functional Theory, *Nano Lett.*, 2024, **24**, 7227–7235.
82 F. Plasser and H. Lischka, Analysis of Excitonic and Charge Transfer Interactions from Quantum Chemical Calculations, *J. Chem. Theory Comput.*, 2012, **8**, 2777–2789.
83 E. Madden, *GitHub*, 2023, DOI: 10.5281/zenodo.10377882.
84 M. Cardona, M. Weinstein and G. A. Wolff, Ultraviolet Reflection Spectrum of Cubic CdS, *Phys. Rev.*, 1965, **140**, A633–A637.
85 J. P. Proot, C. Delerue and G. Allan, Electronic Structure and Optical Properties of Silicon Crystallites: Application to Porous Silicon, *Appl. Phys. Lett.*, 1992, **61**, 1948–1950.
86 H. Fu and A. Zunger, Inp Quantum Dots: Electronic Structure, Surface Effects, and the Redshifted Emission, *Phys. Rev. B:Condens. Matter Mater. Phys.*, 1997, **56**, 1496–1508.
87 F. A. Reboredo, A. Franceschetti and A. Zunger, Dark Excitons Due to Direct Coulomb Interactions in Silicon Quantum Dots, *Phys. Rev. B:Condens. Matter Mater. Phys.*, 2000, **61**, 13073–13087.
88 T. Jeong, P. Yu and T. Kim, Temperature Dependence of the Free Excitons in a CdS Single Crystal, *J. Korean Phys. Soc.*, 2000, **36**, 102–105.
89 C. Bullen and P. Mulvaney, The Effects of Chemisorption on the Luminescence of CdSe Quantum Dots, *Langmuir*, 2006, **22**, 3007–3013.
90 T. Vossmeyer, L. Katsikas, M. Giersig, I. G. Popovic, K. Diesner, A. Chemseddine, A. Eychmueller and H. Weller, CdS Nanoclusters: Synthesis, Characterization, Size Dependent Oscillator Strength, Temperature Shift of the Excitonic Transition Energy, and Reversible Absorbance Shift, *J. Phys. Chem.*, 1994, **98**, 7665–7673.
91 D. Ahlawat, S. Daoud and D. Singh, Electronic, Mechanical, Thermodynamic and Optical Properties of CdS under Pressure, *Indian J. Pure Appl. Phys.*, 2019, **57**, 793–802.

 This journal is © The Royal Society of Chemistry 2025